I-centered versus *F*-centered orthorhombic symmetry and negative thermal expansion of the charge density wave of $EuAl_2Ga_2$

Harshit Agarwal [1,2,*] Surya Rohith Kotla [1] Leila Noohinejad [3] Biplab Bag [4] Claudio Eisele [1] Sitaram Ramakrishnan [5] Martin Tolkiehn [3] Carsten Paulmann [3] Arumugam Thamizhavel [6,†] Srinivasan Ramakrishnan [7,‡] and Sander van Smaalen [1,§]

[1] *Laboratory of Crystallography, University of Bayreuth, 95444 Bayreuth, Germany*
[2] *Institut für Physik, Johannes-Gutenberg-Universität Mainz, 55128 Mainz, Germany*
[3] *Deutsches Elektronen-Synchrotron DESY, Notkestrasse 85, 22607 Hamburg, Germany*
[4] *Department of Physics, Amity Institute of Applied Sciences, Amity University Jharkhand, Ranchi 835303, India*
[5] *I-HUB Quantum Technology Foundation, Indian Institute of Science Education and Research, Pune 411008, India*
[6] *Department of Condensed Matter Physics and Materials Science, TIFR, Mumbai 400005, India*
[7] *Department of Physics, Indian Institute of Science Education and Research, Pune 411008, India*

(Received 24 August 2024; revised 8 March 2025; accepted 11 April 2025; published 24 April 2025)

Together with $EuGa_4$ and $EuAl_4$, $EuAl_2Ga_2$ belongs to the $BaAl_4$ structure type with space group *I*4/*mmm*. $EuAl_2Ga_2$ develops an incommensurate charge density wave (CDW) at temperatures below $T_{CDW} = 51$ K. On the basis of temperature-dependent single-crystal x-ray diffraction data, the incommensurately modulated CDW crystal structure of $EuAl_2Ga_2$ is determined to possess orthorhombic symmetry $Immm(0000\gamma)s0000$. This symmetry is different from the orthorhombic *Fmmm*-based symmetry of the CDW state of $EuAl_4$. Nevertheless, both symmetries, $Immm(00\gamma)s00$ and $Fmmm(00\gamma)s00$, lead to the same conclusion, that the CDW is supported by the layers of Al1 type atoms, while the Eu and Al2 or Ga atoms are not directly involved in CDW formation. The different symmetries of the CDW states of $EuAl_4$ and $EuAl_2Ga_2$, as well as the observation of negative thermal expansion in the CDW state of $EuAl_2Ga_2$, might be explained by the effects of Ga substitution in the latter compound.

DOI: 10.1103/PhysRevB.111.155144

I. INTRODUCTION

Quantum materials have played a significant role in condensed matter research for over a decade, delivering groundbreaking results [1]. Quantum materials refer to a class of materials that exhibit intriguing quantum mechanical properties at the nanoscale or atomic scale [2]. Due to the advent of coupled topological materials [3], our knowledge of emergent processes in quantum materials has improved significantly in recent years [4]. Intermetallic materials with a centrosymmetric square net structural motif having the $BaAl_4$ structure type [5] are ideal examples of quantum materials that exhibit superconductivity (SC), charge density wave (CDW) ordering, antiferromagnetism, and heavy fermionic behavior [6]. In Eu-based intermetallics, Eu can have two types of valence states: Eu^{2+} (magnetic) and Eu^{3+} (nonmagnetic) due to an unstable $4f$ shell. Most Eu-based compounds exist in the divalent Eu^{2+} state and follow the Ruderman–Kittel–Kasuya–Yosida (RKKY) interaction that causes the long-range magnetic ordering [7]. Similarly, Gd^{3+} ($4f^7$, $J = 7/2$, $L = 0$) based centrosymmetric intermetallic compounds follow RKKY interaction, giving rise to Fermi surface nesting [8].

A CDW is a spatial modulation of electron density coupled to a modulation of the atomic positions (periodic lattice modulation, PLD) [9,10]. The origin of CDWs varies between materials but it can be classified according to the dimensionality of the band structure. In quasi-one-dimensional (1D) metals, the stabilization of CDW can be explained by the Peierls model, including Fermi surface nesting, metal-insulator transition, and PLD. In contrast, in two- (2D) and three-dimensional (3D) systems, CDWs occur due to q-dependent electron-phonon coupling, charge ordering, and PLD. However, the structural transition is common in all CDW materials [11]. The PLD leads to satellite reflections at distances $\pm q^{CDW}$ from the main Bragg reflections in single-crystal x-ray diffraction studies (SXRD). The PLD introduces a new periodicity into the crystal and allows the analysis of CDW modulation by SXRD experiments [12]. In 3D systems, first-order phase transition can be observed in physical properties, leading to incommensurate CDW. $EuAl_4$ [13], $SrAl_4$ [14], and $R_2Ir_3Si_5$ (where R = Ho, Er) [15,16] are examples of three-dimensional CDW compounds that show a thermal hysteresis in temperature-dependent electrical resistivity at the CDW transition temperature.

*Contact author: harshit.physics@gmail.com
†Contact author: thamizh@tifr.res.in
‡Contact author: ramky07@gmail.com
§Contact author: smash@uni-bayreuth.de

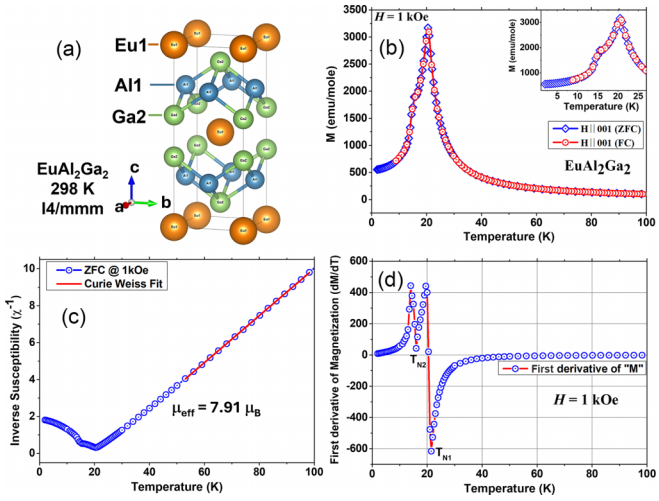

FIG. 1. (a) Tetragonal structure of $EuAl_2Ga_2$ at 298 K having the centrosymmetric *I*4/*mmm* space group. (b) Temperature-dependent dc magnetization measured at a field strength of 1 kOe in the temperature range of 2–100 K for zero-field cooled (ZFC) and field cooled (FC) conditions, showing the antiferromagnetic nature due to Eu^{2+} ion. (c) Inverse susceptibility obtained from the ZFC data; a Curie-Weiss model was fitted to the data between 55 and 100 K (red line). (d) First derivative of magnetization showing the transition temperatures of the material at $T_{N1} \approx 21.4$ K and $T_{N2} \approx 15.8$ K.

Compounds $R(Al_{1-x}Ga_x)_4$ (R = Sr, Eu, Ca) with the tetragonal $BaAl_4$ structure type with space group *I*4/*mmm* have recently received interest, because of the discoveries of tetragonal to orthorhombic CDW transitions in $EuAl_4$ and $SrAl_4$ [14] of a square skyrmion lattice phase in $EuAl_4$ [17–19], and of a tetragonal to monoclinic structural transition in $CaAl_4$ [20,21]. These materials show multiple antiferromagnetic (AFM) transitions with topological Hall effects. Eu-based compounds $Eu(Al_{1-x}Ga_x)_4$ reveal strong correlations between the structural, magnetic, and electronic properties [22,23]. These compounds contain three crystallographically independent atom sites where Ga preferably occupies one of the two independent Al sites [Fig. 1(a)] [23]. $EuAl_4$ exhibits both the CDW at $T_{CDW} = 145$ K and orders antiferromagnetically below $T_{N1} = 15.4$ K with three successive AFM transitions at $T_{N2} = 13.2$ K, $T_{N3} = 12.2$ K, and $T_{N4} = 10.0$ K [24]. However, $EuGa_4$ orders antiferromagnetically below $T_N = 16.4$ K, but it develops a CDW only above a pressure of 2 GPa [24]. $EuAl_4$ contains skyrmionics spin texture; it only requires the alternate stacking of the magnetic Eu layer and nonmagnetic Al layer [25]. Generally, skyrmions appear in noncentrosymmetric materials, but magnetic skyrmion lattice structures have been found in other centrosymmetric compounds, like MnNiGa [26], Gd_2PdSi_3 [27], $GdRu_2Si_2$ [28], and $Gd_3Ru_4Al_{12}$ [29], including $EuAl_2Ga_2$ [22]. Skyrmions can be stabilized in these centrosymmetric compounds without a geometrically frustrated lattice. $BaNi_2As_2$ hosts incommensurate and commensurate CDWs at 142 and 137 K, respectively, and shows symmetry breaking from tetragonal to orthorhombic at 142 K and then a first-order triclinic structural transition at 137 K [30,31]. A phase diagram for $BaNi_2(As_{1-x}P_x)_2$ shows that electronic nematic fluctuations induce a tetragonal to orthorhombic phase transition with the incommensurate charge density wave in the material [32]. The coexistence of CDW and superconductivity is well established in kagome-lattice compounds AV_3Sb_5 (A = K, Rb, Cs) [33], whereas the coexistence of CDW and magnetic order is well established in FeGe [34,35].

The temperature dependence of electrical resistivity shows an anomaly in $EuAl_2Ga_2$, where the Al and Ga atoms split into two sublattices and create an ordered structure, which indicates a CDW state below 51 K [23]. The three-dimensional CDW compound $EuAl_2Ga_2$ follows the RKKY interaction, having four AFM transition temperatures: $T_{N1} \approx 19.5$ K, $T_{N2} \approx 15$ K, $T_{N3} \approx 11$ K, and $T_{N4} \approx 7$ K [22]. It also shows the persistence of the CDW in the magnetically ordered states [22]. The CDW modulation in $EuAl_4$ is orthorhombic with superspace group $Fmmm(00\gamma)s00$ [18]. However, the atomic positions and lattice parameters of the basic structure of the CDW phase obey the tetragonal symmetry [18]. Recent studies on the CDW structure of $EuAl_4$ propose the local symmetry fluctuations from the average symmetry by cryogenic 4D-STM [36]. Alternatively, centrosymmetric $Immm(00\gamma)s00$ superspace group symmetry was proposed for the CDW state of $EuAl_4$ based on inelastic x-ray scattering experiments, but this model does not fit SXRD data [37]. Resonant x-ray scattering (RXS) experiments on $EuGa_2Al_2$ have demonstrated the breaking of fourfold symmetry in the CDW state that can be stabilized orthorhombic domains, either $Immm(00\gamma)s00$ or $Fmmm(00\gamma)s00$ [38]. On the other hand, $SrAl_4$ shows an incommensurate CDW below $T_{CDW} = 243$ K, which has the noncentrosymmetric orthorhombic $F222(00\gamma)00s$ superspace group symmetry with modulation vector $\mathbf{q} = [0, 0, 0.1116(2)]$ at 200 K [39].

A detailed structural description of CDW in $EuAl_2Ga_2$ is presented here. We have found that the CDW state of $EuAl_2Ga_2$ has an incommensurately modulated structure with orthorhombic superspace group $Immm(00\gamma)s00$, which differs from the symmetries of $EuAl_4$ and $SrAl_4$. The presence of CDW modulation below the magnetic transition temperature of $EuAl_2Ga_2$ is also observed.

II. EXPERIMENTAL METHODS

A. Crystal growth

Single crystals of $EuAl_2Ga_2$ were grown by the Al-Ga self-flux method. The elements of europium, aluminum, and gallium were loaded into an alumina crucible in a ratio Eu:Al:Ga = 1:8:4 and subsequently sealed in a quartz-glass ampoule under vacuum. The ampoule was heated to 1173 K, in order to obtain a homogeneous solution. They were cooled at a rate of 2 K/h to 873 K. At 873 K, the ampoules were centrifuged to separate the single crystals from the flux. The stoichiometry of the crystals (i.e., Eu:Al:Ga = 1:2:2) has been confirmed using energy-dispersive x-ray analysis (EDAX).

B. Magnetic properties

The temperature dependence of the magnetic susceptibility of $EuAl_2Ga_2$ was measured on a single crystal using

TABLE I. Crystallographic data of $EuAl_2Ga_2$ at temperatures of 298, 85, 35, 30, and 18 K. The criterion of observability is $I > 3\sigma(I)$. a, b, c are the lattice parameters; V is the volume of the unit cell of the basic structure; and q_z is the z component of the modulation wave vector. D is the detector distance; twvol is twin volume.

Temperature	298 K	85 K	35 K	30 K	18 K
Crystal system	Tetragonal	Tetragonal	Orthorhombic	Orthorhombic	Orthorhombic
Space group	*I*4/*mmm*	*I*4/*mmm*	*Immm*(00γ)*s*00	*Immm*(00γ)*s*00	*Immm*(00γ)*s*00
No.	139	139	71.1.12.2	71.1.12.2	71.1.12.2
Laue symmetry	4/*mmm*	4/*mmm*	*mmm*	*mmm*	*mmm*
a (Å)	4.3389(38)	4.33410(16)	4.29366(14)	4.30768(14)	4.31351(25)
b (Å)	4.3389	4.33410	4.29677(10)	4.31402(13)	4.31411(19)
c (Å)	10.9674(77)	10.95703(47)	10.86970(25)	10.90222(31)	10.91571(54)
V (Å^3)	206.47(41)	205.822(20)	200.534(9)	202.601(12)	203.130(20)
q_z	–	–	0.1142(2)	0.1139 (2)	0.1126(4)
D (mm)	110	260	260	260	260
Filter factor	10.5263	10.5263	1.4804+10.5263	0+10.5263	0+10.5263
2θ offset	0	0, 25	0, 25	0, 25	0, 25
$[\sin(\theta)/\lambda]_{max}$ Å^{-1}	0.690825	0.730126	0.734924	0.732604	0.731724
No. of reflections					
Main (obs/all)	105/108	119/122	153/174	142/161	148/168
Satellites (obs/all)	–	–	179/333	140/331	150/332
R_{int} (obs/all) %	3.67/3.67	1.78/1.78	2.97/3.03	2.33/2.41	2.17/2.22
No. of parameters	9	9	16	16	16
R_F (all) %	1.53	1.60	3.47	3.23	2.50
${}_wR_F^2$ (all) %	1.99	2.12	4.67	3.74	2.85
R_F (main) %	1.53	1.59	2.56	2.63	2.07
R_F (sat) %	–	–	7.84	6.44	4.70
GOF (obs/all)	1.64/1.61	1.66/1.64	1.71/1.41	1.31/1.01	0.98/0.77
twvol1/twvol2	–	–	0.386(8)/0.614	0.419(9)/0.581	0.447(6)/0.552

a commercial superconducting quantum interference device (SQUID) magnetometer (MPMS 7, Quantum Design, USA). Data were obtained after cooling the samples under zero-field cooling (ZFC) and field cooling (FC) conditions. A magnetic field of 1 kOe was applied along the [001] direction of the sample.

C. Single-crystal x-ray diffraction (SXRD)

Temperature-dependent SXRD was carried out at beamline P24 of the synchrotron PETRA-III at DESY in Hamburg. A good-quality single crystal of $EuAl_2Ga_2$ was selected, with dimensions of 0.09 mm × 0.055 mm × 0.018 mm. The SXRD was measured at a Eulerian diffractometer at temperatures down to 18 K using a Cryocool open-flow helium gas cryostat. A Pilatus 1M- CdTe detector was used for data collection. Synchrotron radiation of wavelength 0.5000 Å was used for the experiment. Different runs employed different attenuators in the monochromatized beam, of filter factors of 1, 1.4804, and 10.5263. SXRD data sets were measured for temperatures of 298 and 85 K (tetragonal phase) and of 35, 30, and 18 K (CDW phase). Each run of the data collection contained 3640 frames of $\Delta\varphi = 0.1\,^\circ$ and was repeated 10 times. These data were binned to a data set of 364 frames of 1 ° of rotation and 10 s exposure time per frame, using the programs ADDRUN-SCBF and COMBCBF [40]. A single run at 298 K was recorded at 110 mm crystal to detector distance. Two runs were needed at 35, 30, and 18 K, with and without a 2θ offset, for a 260 mm crystal to detector distance. An improved spatial resolution was achieved at 35, 30, and 18 K through a crystal to detector distance of 270 mm. A similar resolution of the SXRD data then required runs with offsets of 0 ° and 25 ° in 2θ.

CRYSALIS PRO [41] was used to generate undistorted layers of reciprocal space that are based on all of the measured scattering data, including scattering between the Bragg reflections (Fig. 2). The EVAL15 [42] software suite was used for data processing of the binned SXRD data. The two runs with different offsets in 2θ were integrated separately for each of the data measured at 35, 30, and 18 K. They were combined by the module ANY of EVAL15. An outlier rejection was based on tetragonal 4/*mmm* and orthorhombic *mmm* Laue classes. Absorption correction and scaling were performed in SADABS [43] with Laue symmetries 4/*mmm* for all five data sets and *mmm* for the data measured at 35, 30, and 18 K.

The resulting reflection files were imported into JANA2020 [44] for structure solution and refinement. The Laue symmetry 4/*mmm* and *mmm* is used for the periodic and CDW phases of $EuAl_2Ga_2$. We have used the superspace approach to index and integrate the incommensurately modulated data to solve the crystal structure in the CDW phase [12,45]. The crystal structure is drawn using the program VESTA [46].

III. RESULTS AND DISCUSSION

A. Periodic structure and magnetic properties

SXRD data at 298 and 85 K confirmed the $BaAl_4$ structure type with space group *I*4/*mmm* [Table I, Fig. 1(a)]. In this structure, the Eu^{2+} ions form a square layer in the *ab* plane.

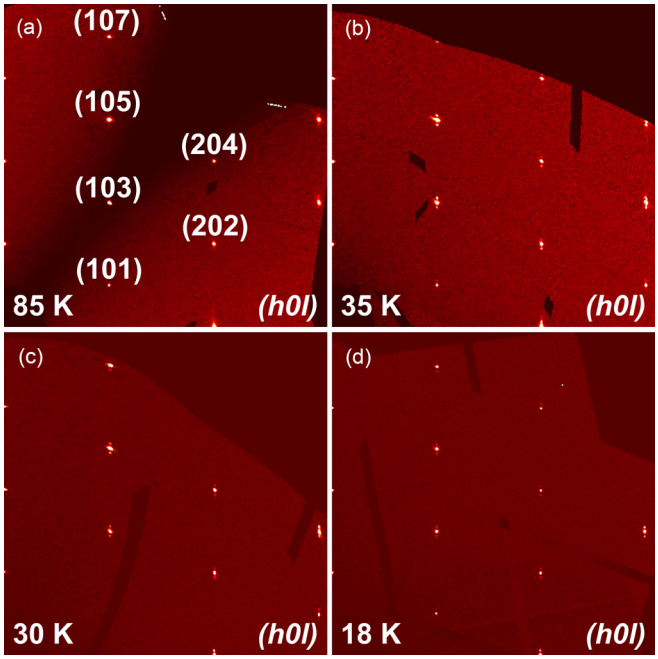

FIG. 2. (*h 0 l*) Sections of reciprocal space reconstructed from SXRD data measured on $EuAl_2Ga_2$ at (a) $T = 85$ K, (b) $T = 35$ K, (c) $T = 30$ K, and (d) $T = 18$ K. Dark areas are due to insensitive parts of the detector.

Neighboring Eu layers are translated by (0.5, 0.5, 0.5) due to the *I* centering. The Al and Ga atoms lie between neighboring Eu layers and are ordered on Wyckoff positions 4*d* and 4*e*, respectively. The refined composition ($EuAl_{2.023\,(21)}Ga_{1.977}$) is close to the nominal composition $EuAl_2Ga_2$. Since Ga thus substitutes for the Al2 atom of $EuAl_4$, the atomic sites in $EuAl_2Ga_2$ are designated as Eu1, Al1, and Ga2. The substitution of Al by Ga results in a reduced volume of $EuAl_2Ga_2$ as compared to $EuAl_4$ [18] and $SrAl_4$ [39].

Previous studies have found that Ga-doped $Eu(Al_{1-x}Ga_x)_4$ compounds exhibit antiferromagnetic transitions below 25 K [23]. Figures 1(b)–1(d) show the temperature-dependent zero-field cooled (ZFC) and field cooled (FC) dc magnetization of $EuAl_2Ga_2$ in the temperature range of 2–100 K, and the presence of 1k Oe magnetic field applied parallel to the *c* axis. The magnetization curve shows an antiferromagnetic nature of the sample where the FC magnetization follows the trend of ZFC magnetization. The inverse susceptibility curve obtained from the ZFC magnetization is shown in Fig. 1(c). A Curie-Weiss fit to the paramagnetic region (55–100 K) resulted in a positive Curie-Weiss temperature that indicates dominant ferromagnetic interactions, despite the antiferromagnetic ordering at lower temperatures. The effective magnetic moment (μ_{eff}) for $EuAl_2Ga_2$ is 7.917 μ_B, which is close to the theoretical value of 7.937 μ_B.

Neutron diffraction studies have provided the incommensurate helical and cycloidal magnetic phases of antiferromagnetic $EuAl_2Ga_2$ below T_N [22]. Multiple magnetic transitions can be identified by anomalies in the temperature dependence of the magnetization and its first derivative. The transition temperatures are $T_{N1} \approx 21.4$ K and $T_{N2} \approx 15.8$ K, for a magnetic field of 1 kOe applied parallel to the *c* axis, as shown in Fig. 1(d). These transition temperatures are very close to those reported by Stavinoha *et al.* [23] and Vibhakar *et al.* [38].

B. Temperature-dependent CDW structure

The first-order, CDW phase transition of $EuAl_2Ga_2$ has been reported to occur at $T_{CDW} \approx 51$ K [22,23]. Figure 2 shows parts of the (*h* 0 *l*) sections of reciprocal space, reconstructed from SXRD data at four different temperatures. First-order satellites are clearly visible along $\mathbf{c}^*$ at 35, 30, and 18 K. They represent the incommensurately modulated CDW with wave vectors $q = [0, 0, 0.1141(2)]$ at 35 K, [0, 0, 0.1139 (2)] at 30 K and [0, 0, 0.1126 (4)] at 18 K. The value of the incommensurate component decreases with decreasing temperature, albeit within a range of 3 times its standard uncertainty. A more complex temperature dependence of the length of the **q** vector was reported by Moya *et al.* [22]. They found a global increase of the length of *q* upon cooling, with a dip (minimum) at T_{N1}. Higher-order satellites were not observed.

We have observed that $EuAl_2Ga_2$ preserves tetragonal *I*4/*mmm* symmetry as symmetry of the basic structure in the CDW state, as was also found for $EuAl_4$ and $SrAl_4$ [18,40]. The incommensurate CDW phase of $EuAl_4$ has the orthorhombic symmetry $Fmmm(00\gamma)s00$ with modulation wave vector $\mathbf{q} = [0, 0, 0.1781(3)]$at 70 K and $\mathbf{q} = [0\ 0\ 0.1741(2)]$ at 20 K [18]. For the CDW phase of $EuAl_2Ga_2$, the present SXRD data indicate symmetry according to the superspace group $Immm(00\gamma)s00$, as detailed below. This finding is in line with the results of resonant inelastic x-ray scattering (RIXS), which indicated the loss of the fourfold symmetry in the CDW state of $EuAl_2Ga_2$ [38].

In order to establish the crystal structure and symmetry of the CDW state of $EuAl_2Ga_2$, the SXRD data were initially processed according to 4/*mmm* point symmetry. Averaging in JANA2020 showed that these SXRD data fulfill 4/*mmm* point symmetry very well according to the observed values of R_{int} (see Table II). However, structure refinements at 35, 30, and 18 K employing a tetragonal superspace group lead to high values for R_F (satellite) (Table II and Tables S4 and S5 [47]). Exception is the superspace group $I422(00\gamma)q00$, but *R* values attained with this noncentrosymmetric superspace group are still significantly higher than those for the orthorhombic choices. Therefore, these results confirm that the CDW phase does not have tetragonal symmetry. Secondly, structure models were employed with superspace groups based on orthorhombic subgroups of I4/*mmm*. SXRD data processed in 4/*mmm* symmetry imply two orthorhombic domains with twin fractions 0.5:0.5. Structure refinements then led to comparable *R* values for orthorhombic superspace groups $Fmmm(00\gamma)s00$ and $Immm(00\gamma)s00$ (Table II).

In a second approach, structure refinements of models with $Fmmm(00\gamma)s00$ and $Immm(00\gamma)s00$ symmetries have been performed against the SXRD data processed according to the respective orthorhombic point symmetries *Fmmm* and *Immm*. Here, *R* values indicate a better fit for $Immm(00\gamma)s00$ than for $Fmmm(00\gamma)s00$ for all the temperatures (Table II). Volumes for the twin domains were refined and they deviate significantly from 0.5:0.5 for the structure in $Immm(00\gamma)s00$

TABLE II. R values (%) of different structure models on the basis of different centrosymmetric and noncentrosymmetric superspace groups for SXRD data at 35, 30, and 18 K.

Superspace group	Averaging	R_{int}	R_F (All)	R_F (Main)	R_F (Satellite)	${}_wR_F^2$(All)	Number of reflections (Main/satellite)	Parameter
				Temperature = 35 K				
$I4/mmm(00\gamma)000$	$4/mmm$	3.28	12.73	3.12	59.91	19.92	99/105	13
$Fmmm(00\gamma)s00$	$4/mmm$	3.28	3.02	1.91	8.46	3.56	99/105	14
$Immm(00\gamma)s00$	$4/mmm$	3.28	2.98	1.90	8.30	3.58	99/105	15
$Fmmm(00\gamma)s00$	mmm	2.77	3.59	2.40	9.57	4.39	147/161	15
$F222(00\gamma)00s$	mmm	2.77	3.55	2.39	9.38	4.36	147/161	19
$Immm(00\gamma)s00$	mmm	2.97	3.47	2.56	7.84	4.67	153/179	16
$I222(00\gamma)00s$	mmm	2.97	3.46	2.56	7.76	4.66	153/179	20
$I422(00\gamma)q00$	mmm	2.97	3.82	2.67	9.36	5.47	153/179	14
				Temperature = 30 K				
$I4/mmm(00\gamma)000$	$4/mmm$	2.88	15.31	4.75	64.98	23.98	92/105	13
$Fmmm(00\gamma)s00$	$4/mmm$	2.88	2.77	1.96	6.53	3.31	92/105	14
$Immm(00\gamma)s00$	$4/mmm$	2.88	2.75	1.97	6.43	3.35	92/105	15
$Fmmm(00\gamma)s00$	mmm	2.89	3.82	2.82	8.60	4.66	148/162	15
$F222(00\gamma)00s$	mmm	2.89	3.76	2.80	8.46	4.63	148/162	19
$Immm(00\gamma)s00$	mmm	2.33	3.24	2.63	6.45	3.74	142/140	16
$I222(00\gamma)00s$	mmm	2.33	3.22	2.63	6.37	3.74	142/140	20
$I422(00\gamma)q00$	mmm	2.33	3.39	2.64	7.39	3.99	142/140	14
				Temperature = 18 K				
$I4/mmm(00\gamma)000$	$4/mmm$	2.69	12.66	2.88	59.68	19.70	97/105	13
$Fmmm(00\gamma)s00$	$4/mmm$	2.69	2.13	1.56	4.85	2.45	97/105	14
$Immm(00\gamma)s00$	$4/mmm$	2.69	2.13	1.56	4.85	2.47	97/105	15
$Fmmm(00\gamma)s00$	mmm	2.60	2.91	2.27	6.12	3.31	151/150	15
$F222(00\gamma)00s$	mmm	2.60	2.87	2.27	5.92	3.28	151/150	19
$Immm(00\gamma)s00$	mmm	2.17	2.50	2.07	4.71	2.86	148/150	16
$I222(00\gamma)00s$	mmm	2.17	2.49	2.07	4.64	2.85	148/150	20
$I422(00g)q00$	mmm	2.17	2.59	2.11	5.05	3.01	148/150	14

(Table I). Table III provides the basic-structure coordinates of $EuAl_2Ga_2$ at 298 and 85 K with $I4/mmm$ symmetry, and at 35, 30, and 18 K with orthorhombic $Immm(00\gamma)s00$ symmetry. The basic structure of $EuAl_2Ga_2$ retains tetragonal symmetry

TABLE III. Atomic coordinates of $EuAl_2Ga_2$ as obtained from structure refinements against SXRD data at 298 and 85 K (crystal structure), and at 35, 30, and 18 K (basic structure).

Atoms	x	y	z	$U11$	$U22$	$U33$	$U12$	$U13$	$U23$	U_{eq}
					298 K ($I4/mmm$)					
Eu1	0	0	0	0.0087(3)	0.0087(3)	0.0096(3)	0	0	0	0.0090(1)
Al1	0	0.5	0.25	0.0085(5)	0.0085(5)	0.0067(7)	0	0	0	0.0079(3)
Ga2	0	0	0.38561(6)	0.0112(3)	0.0112(3)	0.0073(4)	0	0	0	0.0073(4)
					85 K ($I4/mmm$)					
Eu1	0	0	0	0.0030(2)	0.0030(2)	0.0039(3)	0	0	0	0.0033(1)
Al1	0	0.5	0.25	0.0030(5)	0.0030(5)	0.0031(7)	0	0	0	0.0030(3)
Ga2	0	0	0.38564(6)	0.0045(3)	0.0045(3)	0.0041(3)	0	0	0	0.0043(1)
					35 K [$Immm(00\gamma)s00$]					
Eu1	0	0	0	0.0032(3)	0.0032(3)	0.0034(4)	0	0	0	0.0033(2)
Al1	0	0.5	0.2514(8)	0.0030(10)	0.0030(10)	0.0011(14)	0	0	0	0.0024(5)
Ga2	0	0	0.38566(9)	0.0040(4)	0.0040(4)	0.0031(5)	0	0	0	0.0037(2)
					30 K [$Immm(00\gamma)s00$]					
Eu1	0	0	0	0.0047(3)	0.0047(3)	0.0037(3)	0	0	0	0.00433(17)
Al1	0	0.5	0.2497(10)	0.0025(9)	0.0025(9)	0.0010(12)	0	0	0	0.0020(6)
Ga2	0	0	0.38562(8)	0.0059(4)	0.0059(4)	0.0032(4)	0	0	0	0.0050(2)
					18 K [$Immm(00\gamma)s00$]					
Eu1	0	0	0	0.0031(2)	0.0031(2)	0.0019(2)	0	0	0	0.00271(12)
Al1	0	0.5	0.2486(7)	0.0025(6)	0.0025(6)	0.0001(8)	0	0	0	0.0017(4)
Ga2	0	0	0.38565(6)	0.0045(3)	0.0045(3)	0.0017(3)	0	0	0	0.00358(16)

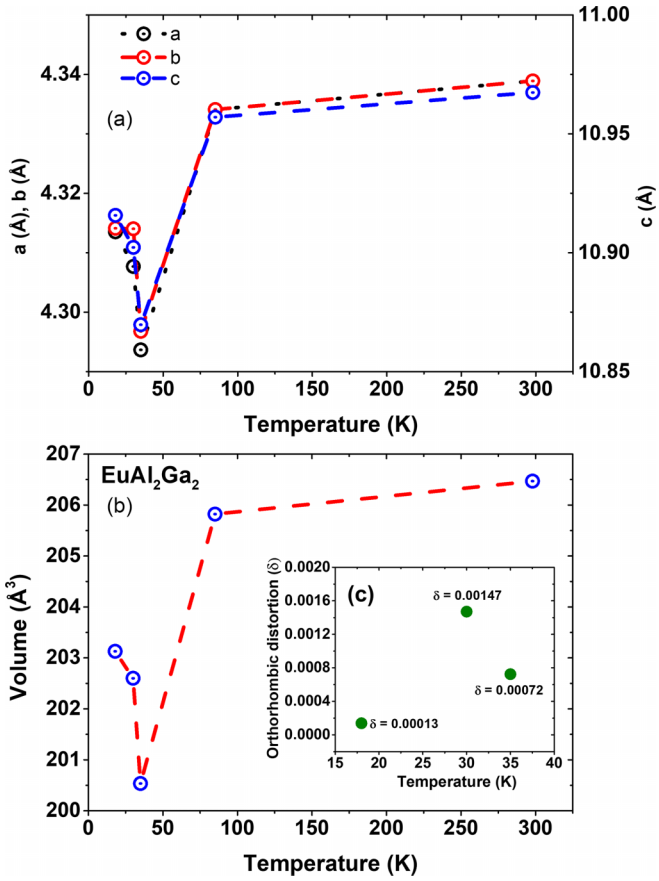

FIG. 3. Temperature dependence of the (a) lattice parameters and (b) volume of the unit cell, and, in the inset (c), orthorhombic distortion, computed as $\delta = 2(b-a)/(b+a)$, where a, b, and c are the orthorhombic lattice parameters. The standard uncertainties in the lattice parameters are smaller than the size of the data points; refer to Table I.

at all temperatures, since the z coordinate of Al1 does not deviate significantly from 0.25. Details on the structure model with $Fmmm(00\gamma)s00$ symmetry are proved in Tables S1–S3 in the Supplemental Material [47].

Recently we found for $SrAl_4$ that a noncentrosymmetric structure with symmetry $F222(00\gamma)00s$ gives a better fit to the SXRD data than its supergroup $Fmmm(00\gamma)s00$ [36,39]. The main argument was a better fit to the second-order satellites for the noncentrosymmetric model [39]. For $EuAl_4$, the SXRD data set did not contain second-order satellites, and the centrosymmetric and noncentrosymmetric models could not be distinguished [18,39]. Presently, without second-order satellites for $EuAl_2Ga_2$, noncentrosymmetric superspace groups do lead to better fits to the data than the superspace group $Immm(00\gamma)s00$ (Table II). Furthermore, refinements are unstable for superspace groups based on point symmetry 222, thus indicating dependencies between the parameters. A complete list of noncentrosymmetric space groups for 18 K is shown in Table S4 of the Supplemental Material [47]. In conclusion, the present SXRD data lead to a centrosymmetric structure model for the CDW state of $EuAl_2Ga_2$, which has orthorhombic symmetry $Immm(00\gamma)s00$.

C. Thermal expansion

The temperature dependence of each lattice parameter follows the same trend as the overall unit cell volume as shown in Figs. 3(a) and 3(b). The present data reveal negative thermal expansion (NTE) below the CDW transition (Table I). Also, the orthorhombic distortion (δ) shown in Fig. 3(c) as a plot of $[2(b-a)/(a+b)]$ versus temperature suggests an increase of orthorhombic distortion on cooling within the CDW phase, while the orthorhombic distortion becomes much smaller below T_{N_1}. The latter effect agrees with the decreased intensity of satellite reflections below T_{N1} [22], which would indicate a weaker CDW within the magnetically ordered phases.

It has been shown that NTE can be enhanced by substituting Al, Ga, and Cr in various intermetallics [48], which also enhances the magnetic transition temperature [49]. The substitution of Al with Ga alters the Eu–Eu interatomic distances, thereby modifying the magnetic exchange interactions and resulting in magnetic ordering at a higher temperature. NTE has been found in other RT_2X_2 compounds like the $YbMn_2Ge_2$ compound over a wide temperature range which is due to electron driven NTE effects such as valence transition and magnetovolume effect [50]. The proposed mechanism

TABLE IV. Amplitudes of the modulation functions of structure models for $EuAl_2Ga_2$ at 35, 30, and 18 K, for the superspace group $Immm(00\gamma)s00$.

Atoms	$A_{1,x}a$ (Å)	$A_{1,y}b$ (Å)	$A_{1,z}c$ (Å)	$B_{1,x}a$ (Å)	$B_{1,y}b$ (Å)	$B_{1,z}c$ (Å)
			35 K [$Immm(00\gamma)s00$]			
Eu1	0.07979(35)	0	0	0	0	0
Al1	0.07629(133)	0	0	–0.02742(155)	0	0
Ga2	0.07999(56)	0	0	0.02860(45)	0	0
			30 K [$Immm(00\gamma)s00$]			
Eu1	0.07804(38)	0	0	0	0	0
Al1	0.07420(139)	0	0	–0.02489(170)	0	0
Ga2	0.07968(61)	0	0	0.02864(51)	0	0
			18 K [$Immm(00\gamma)s00$]			
Eu1	0.07987(28)	0	0	0	0	0
Al1	0.07869(115)	0	0	–0.02435(132)	0	0
Ga2	0.07975(45)	0	0	0.02813(39)	0	0

of NTE can be the effect of magnetism and valence transition, as observed in $YbMn_2Ge_2$, and chemical diversity [51]. The NTEs $[\alpha_V = \frac{1}{V}(\frac{dV}{dT})]$ in $EuAl_2Ga_2$ at the temperature difference of 35–30 K and 30–18 K are $-2.06 \times 10^{-3}\,K^{-1}$ and $-2.17 \times 10^{-4}\,K^{-1}$ observed with space group $Immm(00\gamma)s00$. We have also observed an increase in volume at lower temperatures below the CDW transition temperature for the $Fmmm(00\gamma)s00$ symmetry [47]. The magnetic transition temperature in $EuAl_2Ga_2$ increases to ∼21.6 K in comparison to $EuAl_4$ at ∼15 K due to the presence of Ga and the valence transition of Eu^{3+} to Eu^{2+}. These features thus explain the observation of the NTE of $EuAl_2Ga_2$ due to the presence of Ga substitution at the Al site of $EuAl_4$. However, more studies are necessary for confirming this conjecture.

D. Location of the CDW

Structural parameters, such as atomic displacements, atomic distances, and bond angles, can be evaluated as a function of the phase t of the modulation wave. Such t plots are useful for analyzing the correlated variations of different parameters, e.g., of the atomic environments. The displacement modulation is described by a modulation function for each atom of the form [12]

$$u_\alpha(\bar{x}_{s4}) = \sum_n \{A_{\alpha,n} \sin(2n\pi\ \bar{x}_{s4}) + B_{\alpha,\,n} \cos(2n\pi\ \bar{x}_{s4})\}, \tag{1}$$

where $n = 1$ due to first-order harmonics and $\alpha = x, y, z$. The fourth superspace coordinate for the jth atom can be represented as $\bar{x}_{s4}(j) = t + \boldsymbol{q} \cdot \bar{\boldsymbol{x}}(j)$ where t is the initial phase of modulation and $\bar{\boldsymbol{x}}(j)$ is the position of the jth atom in the periodic basic structure. $A_{\alpha,n}$ and $B_{\alpha,\,n}$ are amplitude coefficients for each harmonic component along the α direction (x, y, z) [12]. The observed amplitudes for displacement modulation show that atoms have displacements (u_x) along the x direction and zero displacements u_y along y and u_z along z for the structure models with superspace group $Immm(00\gamma)s00$ [Table IV and Figs. 4(a)–4(c)]. The nonzero modulation amplitudes for all three atoms contribute to CDW order in the material. However, the Eu1 atom is elastically coupled to Al1 and Ga2 atoms, having the sine component of modulation function, whereas Al1 and Ga2 have periodic components of both sine and cosine waves along the x direction. Displacement modulation for all the atoms is a transverse wave.

To understand how Al1 and Ga2 atoms contribute to CDW ordering in the material, we consider the shortest interatomic distances, which are Ga2–Ga2, Ga2–Al1, and Al1–Al1 distances. t plots of these interatomic distances show that the largest modulation is found for the Al1–Al1 distances at all three temperatures (Figs. 5 and 6 and Figs. S1–S3 [47]). This finding suggests that the CDW resides on the Al atoms, like for $EuAl_4$ [18]. The CDW structure with I-centered orthorhombic symmetry exhibits the same variation of Al1-Al1 bond distance but with approximately half the amplitude observed in the F-centered orthorhombic structure of $EuAl_4$. The different symmetries of the CDWs in $EuAl_2Ga_2$ and $EuAl_4$ [18] can be attributed to the presence of Ga in $EuAl_2Ga_2$.

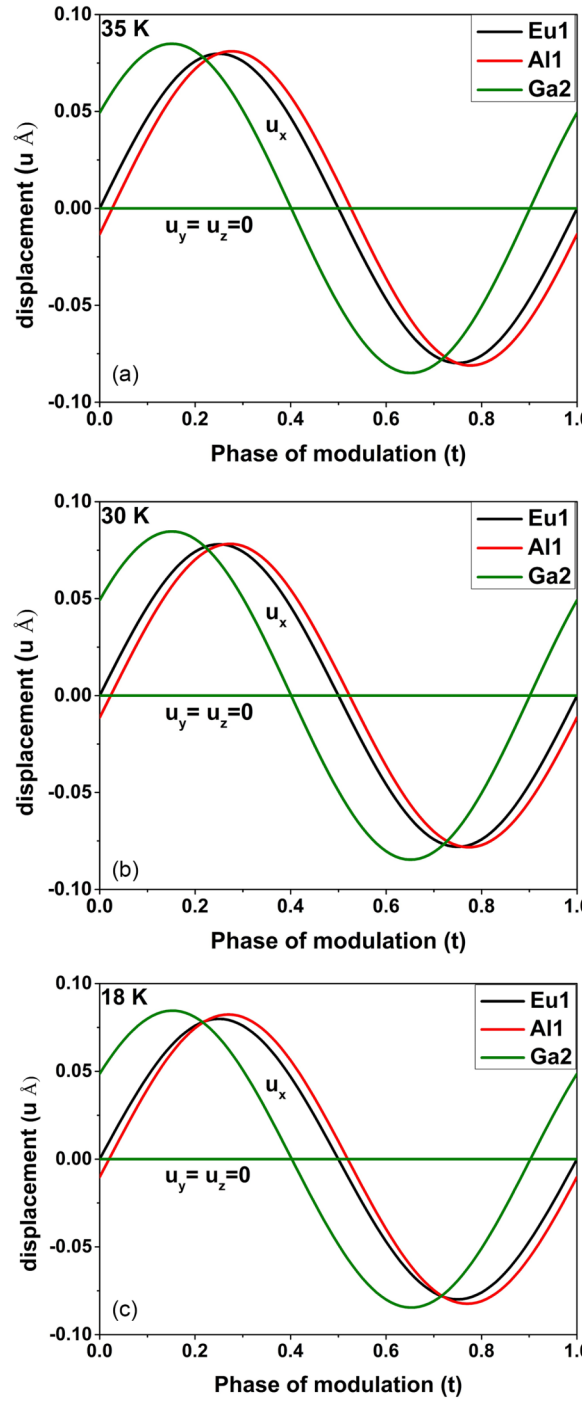

FIG. 4. t plot of the modulation functions for the displacement of atoms Eu1, Al1, and Ga2 at 35, 30, and 18 for superspace group $Immm(00\gamma)s00$. Amplitudes of the modulation functions with standard deviation for Eu, Al, and Ga atoms are mentioned in Table IV.

IV. CONCLUSIONS

Like $EuGa_4$, $EuAl_4$, and $SrAl_4$, $EuAl_2Ga_2$ has the $BaAl_4$ structure type with tetragonal symmetry $I4/mmm$ at room temperature. SXRD shows the presence of satellite reflections along $\mathbf{c}^*$ at temperatures below $T_{CDW} = 51$ K. The incommensurately modulated CDW crystal structure of $EuAl_2Ga_2$ was found to possess symmetry according to the superspace

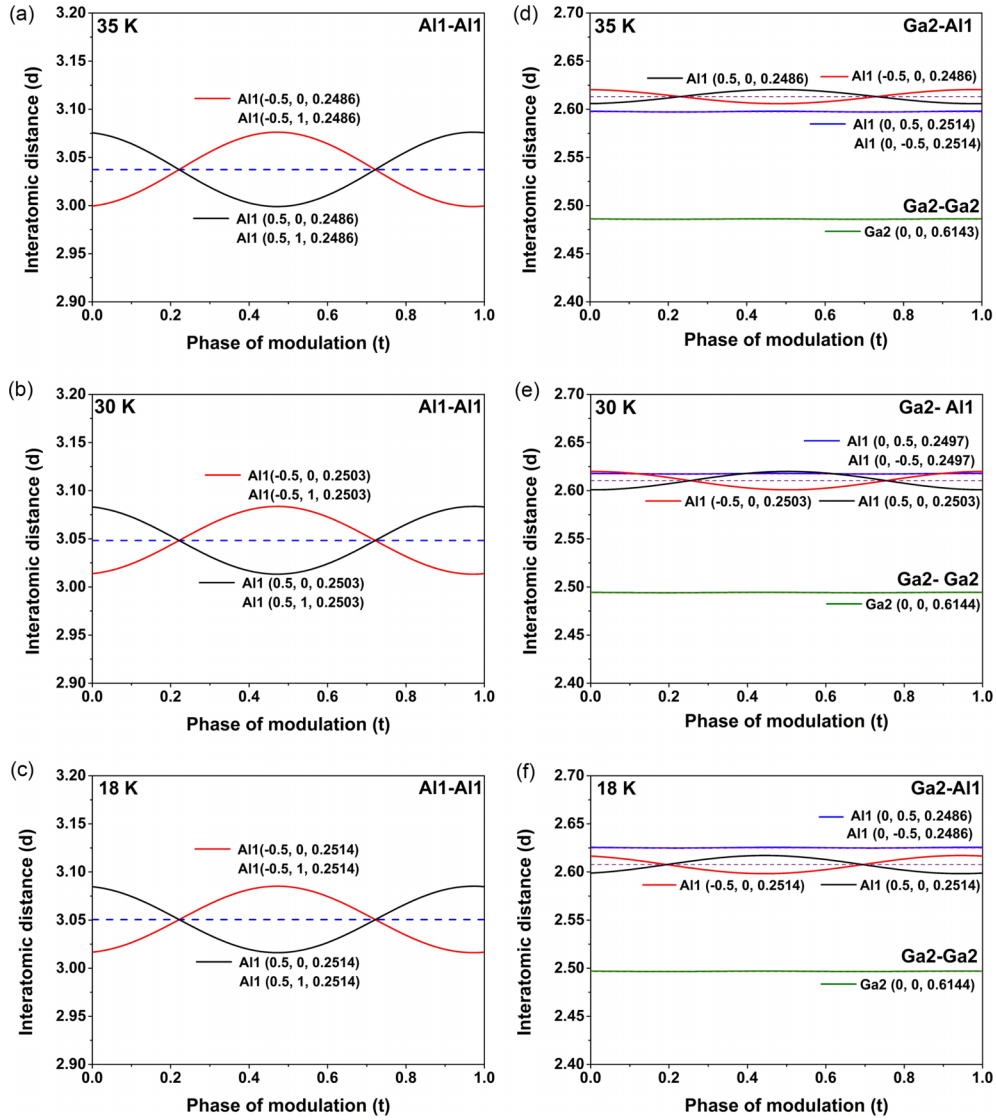

FIG. 5. t plot of interatomic distances (Å) d[Al1 − Al1], d[Ga2 − Al1], d[Ga2 − Ga2] at 35, 30, and 18 K for superspace group $Immm(00\gamma)s00$. Compare to Fig. 6.

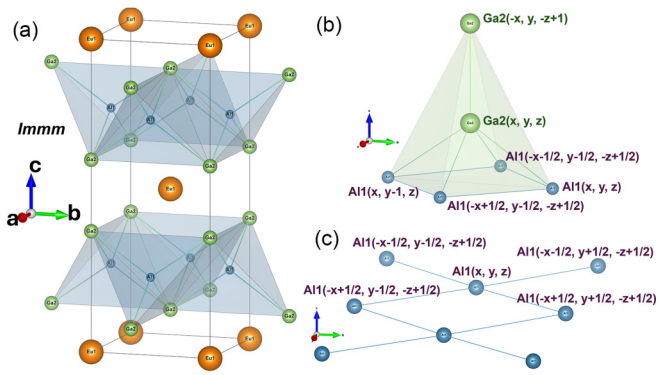

FIG. 6. Crystal structure of $EuAl_2Ga_2$ having orthorhombic structure with *Immm* symmetry at 18 K. (a) Polyhedral view of Al1-Ga2 atoms. (b) Neighboring atoms of Ga2 for which the CDW modes between Ga2-Ga2 and Ga2-Al1 atoms are shown in Fig. 5. (c) Neighboring Al atoms of Al1 for which the Al1-Al1 layers show the largest modulation of interatomic distances causing CDW in the material.

group $Immm(00\gamma)s00$. This is different from $EuAl_4$ that has superspace symmetry $Fmmm(00\gamma)s00$ for its CDW state, and it is different from $EuGa_4$, which does not develop a CDW at ambient pressure. The different symmetries of the CDW states of $EuAl_4$ and $EuAl_2Ga_2$ might thus be explained by the effects of Ga substitution in the latter compound. In this respect, it should be noted that both structure models, $Fmmm(00\gamma)s00$ and $Immm(00\gamma)s00$, lead to a large variation of the Al1–Al1 contact distance as a principal effect of the modulation. Either model thus explains the presence of the CDW on the Al1 atoms. We have found negative thermal expansion (NTE) below T_{CDW}. The NTE effect can be rationalized as the result of Ga substitution into this intermetallic material [45].

ACKNOWLEDGMENTS

We thank Kerstin Küspert and Franz Fischer for technical assistance with the experiments. We acknowledge Deutsches Elektronen-Synchrotron (DESY) (Hamburg, Germany), a member of the Helmholtz Association HGF, for the provision

of experimental facilities. Parts of this research were carried out at PETRA-III, and we would like to thank Heiko Schulz-Ritter for assistance in using beamline P24. Beam time was allocated for Proposal No. I-20211203.

DATA AVAILABILITY

The data that support the findings of this article are not publicly available. The data are available from the authors upon reasonable request.

[1] F. Giustino, J. H. Lee, F. Trier, M. Bibes, S. M. Winter, R. Valentí, Y.-W. Son, L. Taillefer, C. Heil, A. I. Figueroa *et al.*, The 2021 quantum materials roadmap, J. Phys. Mater. **3**, 042006 (2020).

[2] D. N. Basov, R. D. Averitt, and D. Hsieh, Towards properties on demand in quantum materials, Nat. Mater. **16**, 1077 (2017).

[3] N. Kumar, S. N. Guin, K. Manna, C. Shekhar, and C. Felser, Topological quantum materials from the viewpoint of chemistry, Chem. Rev. **121**, 2780 (2021).

[4] B. A. Bernevig, C. Felser, and H. Beidenkopf, Progress and prospects in magnetic topological materials, Nature (London) **603**, 41 (2022).

[5] S. Klemenz, A. K. Hay, S. M. L. Teicher, A. Topp, J. Cano, and L. M. Schoop, The role of delocalized chemical bonding in square-net-based topological semimetals, J. Am. Chem. Soc. **142**, 6350 (2020).

[6] M. Shatruk, $ThCr_2Si_2$ structure type: The "perovskite" of intermetallics, J. Solid State Chem. **272**, 198 (2019).

[7] S. D. Ramarao, A. K. Singh, U. Subbarao, and S. C. Peter, An overview on the structural diversity of europium based ternary intermetallics, J. Solid State Chem. **281**, 121048 (2020).

[8] J. Bouaziz, E. Mendive-Tapia, S. Blügel, and J. B. Staunton, Fermi-surface origin of skyrmion lattices in centrosymmetric rare-earth intermetallics, Phys. Rev. Lett. **128**, 157206 (2022).

[9] J. P. Pouget and E. Canadell, Structural approach to charge density waves in low-dimensional systems: Electronic instability and chemical bonding, Rep. Prog. Phys. **87**, 026501 (2024).

[10] X. Zhu, Y. Cao, J. Zhang, E. W. Plummer, and J. Guo, Classification of charge density waves based on their nature, Proc. Natl. Acad. Sci. USA **112**, 2367 (2015).

[11] X. Zhu, J. Guo, J. Zhang, and E. W. Plummer, Misconceptions associated with the origin of charge density waves, Adv. Phys. X **2**, 622 (2017).

[12] S. van Smaalen, *Incommensurate Crystallography* (Oxford University Press, Oxford, 2007).

[13] W. R. Meier, J. R. Torres, R. P. Hermann, J. Zhao, B. Lavina, B. C. Sales, and A. F. May, Thermodynamic insights into the intricate magnetic phase diagram of $EuAl_4$, Phys. Rev. B **106**, 094421 (2022).

[14] A. Nakamura, T. Uejo, H. Harima, S. Araki, T. C. Kobayashi, M. Nakashima, Y. Amako, M. Hedo, T. Nakama, and Y. Onuki, Characteristic Fermi surfaces and charge density wave in $SrAl_4$ and related compounds with the $BaAl_4$-type tetragonal structure, J. Alloys Compd. **654**, 290 (2016).

[15] S. Ramakrishnan, J. Bao, C. Eisele, B. Patra, M. Nohara, B. Bag, L. Noohinejad, M. Tolkiehn, C. Paulmann, A. M. Schaller *et al.*, Coupling between charge density wave ordering and magnetism in $Ho_2Ir_3Si_5$, Chem. Mater. **35**, 1980 (2023).

[16] S. Ramakrishnan, A. Schönleber, T. Rekis, N. van Well, L. Noohinejad, S. van Smaalen, M. Tolkiehn, C. Paulmann, B. Bag, A. Thamizhavel, D. Pal, and S. Ramakrishnan, Unusual charge density wave transition and absence of magnetic ordering in $Er_2Ir_3Si_5$, Phys. Rev. B **101**, 060101(R) (2020).

[17] S. Shimomura, H. Murao, S. Tsutsui, H. Nakao, A. Nakamura, M. Hedo, T. Nakama, and Y. Ōnuki, Lattice modulation and structural phase transition in the antiferromagnet $EuAl_4$, J. Phys. Soc. Jpn. **88**, 014602 (2019).

[18] S. Ramakrishnan, S. R. Kotla, T. Rekis, J. K. Bao, C. Eisele, L. Noohinejad, M. Tolkiehn, C. Paulmann, B. Singh, R. Verma *et al.*, Orthorhombic charge density wave on the tetragonal lattice of $EuAl_4$, IUCrJ **9**, 378 (2022).

[19] M. Gen, R. Takagi, Y. Watanabe, S. Kitou, H. Sagayama, N. Matsuyama, Y. Kohama, A. Ikeda, Y. Ōnuki, T. Kurumaji, T. H. Arima, and S. Seki, Rhombic skyrmion lattice coupled with orthorhombic structural distortion in $EuAl_4$, Phys. Rev. B **107**, L020410 (2023).

[20] G. J. Miller, F. Li, and H. F. Franzen, The structural phase transition in $CaAl_4$: A concerted application of Landau theory and energy band theory, J. Am. Chem. Soc. **115**, 3739 (1993).

[21] S. Engel, E. C. J. Gießelmann, L. E. Schank, G. Heymann, K. Brix, R. Kautenburger, H. P. Beck, and O. Janka, Theoretical and ^{27}Al NMR spectroscopic investigations of binary intermetallic alkaline-earth aluminides, Inorg. Chem. **62**, 4260 (2023).

[22] J. M. Moya, S. Lei, E. M. Clements, C. S. Kengle, S. Sun, K. Allen, Q. Li, Y. Y. Peng, A. A. Husain, M. Mitrano *et al.*, Incommensurate magnetic orders and topological Hall effect in the square-net centrosymmetric $EuGa_2Al_2$ system, Phys. Rev. Mater. **6**, 074201 (2022).

[23] M. Stavinoha, J. A. Cooley, S. G. Minasian, T. M. McQueen, S. M. Kauzlarich, C. L. Huang, and E. Morosan, Charge density wave behavior and order-disorder in the antiferromagnetic metallic series $Eu(Ga_{1-x}Al_x)_4$, Phys. Rev. B **97**, 195146 (2018).

[24] A. Nakamura, T. Uejo, F. Honda, T. Takeuchi, H. Harima, E. Yamamoto, Y. Haga, K. Matsubayashi, Y. Uwatoko, M. Hedo, T. Nakama, and Y. O'Nuki, Transport and magnetic properties of $EuAl_4$ and $EuGa_4$, J. Phys. Soc. Jpn. **84**, 124711 (2015).

[25] R. Takagi, N. Matsuyama, V. Ukleev, L. Yu, J. S. White, S. Francoual, J. R. L. Mardegan, S. Hayami, H. Saito, K. Kaneko *et al.*, Square and rhombic lattices of magnetic skyrmions in a centrosymmetric binary compound, Nat. Commun. **13**, 1 (2022).

[26] W. Wang, Y. Zhang, G. Xu, L. Peng, B. Ding, Y. Wang, Z. Hou, X. Zhang, X. Li, E. Liu *et al.*, A centrosymmetric hexagonal magnet with superstable biskyrmion magnetic nanodomains in a wide temperature range of 100–340 K, Adv. Mater. **28**, 6887 (2016).

[27] T. Kurumaji, T. Nakajima, M. Hirschberger, A. Kikkawa, Y. Yamasaki, H. Sagayama, H. Nakao, Y. Taguchi, T. hisa Arima, and Y. Tokura, Skyrmion lattice with a giant topological Hall effect in a frustrated triangular-lattice magnet, Science **365**, 914 (2019).

[28] G. D. A. Wood, D. D. Khalyavin, D. A. Mayoh, J. Bouaziz, A. E. Hall, S. J. R. Holt, F. Orlandi, P. Manuel, S. Blügel, J. B. Staunton *et al.*, Double-Q ground state with topological charge stripes in the centrosymmetric skyrmion candidate $GdRu_2Si_2$, Phys. Rev. B **107**, L180402 (2023).

[29] M. Hirschberger, T. Nakajima, S. Gao, L. Peng, A. Kikkawa, T. Kurumaji, M. Kriener, Y. Yamasaki, H. Sagayama, H. Nakao *et al.*, Skyrmion phase and competing magnetic orders on a breathing kagomé lattice, Nat. Commun. **10**, 1 (2019).

[30] M. Merz, L. Wang, T. Wolf, P. Nagel, C. Meingast, and S. Schuppler, Rotational symmetry breaking at the incommensurate charge-density-wave transition in $Ba(Ni, Co)_2(As, P)_2$: Possible nematic phase induced by charge/orbital fluctuations, Phys. Rev. B **104**, 184509 (2021).

[31] Y. Yao, R. Willa, T. Lacmann, S.-M. Souliou, M. Frachet, K. Willa, M. Merz, F. Weber, C. Meingast, R. Heid *et al.*, An electronic nematic liquid in $BaNi_2As_2$, Nat. Commun. **13**, 4535 (2022).

[32] M. Frachet, P. Wiecki, T. Lacmann, S. M. Souliou, K. Willa, C. Meingast, M. Merz, A. A. Haghighirad, M. Le Tacon, and A. E. Böhmer, Elastoresistivity in the incommensurate charge density wave phase of $BaNi_2(As_{1-x}P_x)_2$, npj Quantum Mater. **7**, 1 (2022).

[33] L. Kautzsch, B. R. Ortiz, K. Mallayya, J. Plumb, G. Pokharel, J. P. C. Ruff, Z. Islam, E.-A. Kim, R. Seshadri, and S. D. Wilson, Structural evolution of the kagome superconductors AV_3Sb_5 (A = K, Rb, and Cs) through charge density wave order, Phys. Rev. Mater. **7**, 024806 (2023).

[34] C. Shi, Y. Liu, B. B. Maity, Q. Wang, S. R. Kotla, S. Ramakrishnan, C. Eisele, H. Agarwal, L. Noohinejad, Q. Tao *et al.*, Annealing-induced long-range charge density wave order in magnetic kagome FeGe: Fluctuations and disordered structure, Sci. China Phys., Mech. Astron. **67**, 117012 (2024).

[35] C. Shi, H. Deng, S. R. Kotla, Y. Liu, S. Ramakrishnan, C. Eisele, H. Agarwal, L. Noohinejad, J.-Y. Liu, T. Yang *et al.*, Charge density wave without long-range structural modulation in canted antiferromagnetic kagome FeGe, arXiv:2404.00996.

[36] H. Ni, W. R. Meier, H. Miao, A. F. May, B. C. Sales, J. M. Zuo, and M. Chi, Real-space visualization of atomic displacements in a long-wavelength charge density wave using cryogenic 4D-STEM, Phys. Rev. Mater. **8**, 104414 (2024).

[37] A. N. Korshunov, A. S. Sukhanov, S. Gebel, M. S. Pavlovskii, N. D. Andriushin, Y. Gao, J. M. Moya, E. Morosan, and M. C. Rahn, Phonon softening and atomic modulations in $EuAl_4$, Phys. Rev. B **110**, 045102 (2024).

[38] A. M. Vibhakar, D. D. Khalyavin, J. M. Moya, P. Manuel, F. Orlandi, S. Lei, E. Morosan, and A. Bombardi, Competing charge and magnetic order in the candidate centrosymmetric skyrmion host $EuGa_2Al_2$, Phys. Rev. B **108**, L100404 (2023).

[39] S. Ramakrishnan, S. R. Kotla, H. Pi, B. B. Maity, J. Chen, J. K. Bao, Z. Guo, M. Kado, H. Agarwal, C. Eisele *et al.*, Non-centrosymmetric, transverse structural modulation in $SrAl_4$, and elucidation of its origin in the BaAl4 family of compounds, Phys. Rev. Res. **6**, 023277 (2024).

[40] C. Paulmann and M. Tolkiehn, Binning software: ADDRUNSCBF, COMBCBF, for averaging fine slicing frames and dead time correction Pilatus and Lambda detector, *PETRA III, DESY* (2023).

[41] Agilent Technologies, UK, CRYSALIS PRO: Data collection and data reduction GUI, Version 171.43.131a, Rigaku Oxford Diffraction (2024).

[42] A. M. M. Schreurs, X. Xian, and L. M. J. Kroon-Batenburg, EVAL15: A diffraction data integration method based on *ab initio* predicted profiles, J. Appl. Crystallogr. **43**, 70 (2010).

[43] L. Krause, R. Herbst-Irmer, G. M. Sheldrick, and D. Stalke, Comparison of silver and molybdenum microfocus x-ray sources for single-crystal structure determination, J. Appl. Crystallogr. **48**, 3 (2015).

[44] V. Petříček, L. Palatinus, J. Plášil, and M. Dušek, JANA2020—A new version of the crystallographic computing system JANA, Z. Kristallogr. - Cryst. Mater. **238**, 271 (2023).

[45] A. Janner and T. Janssen, Symmetry of incommensurate crystal phases. I. Commensurate basic structures, Acta Crystallogr., Sect. A **36**, 399 (1980).

[46] K. Momma and F. Izumi, VESTA: A three-dimensional visualization system for electronic and structural analysis, J. Appl. Crystallogr. **41**, 653 (2008).

[47] See Supplemental Material at http://link.aps.org/supplemental/10.1103/PhysRevB.111.155144 for SXRD data reduction, symmetry of the incommnesurate phase at 18 K, and t plots of $EuAl_2Ga_2$ along with the magnetization study of $Eu(Al_{1-x}Ga_x)_4$.

[48] K. Takenaka, Negative *thermal* expansion materials: Technological key for control of thermal expansion, Sci. Technol. Adv. Mater. **13**, 013001 (2012).

[49] J. Chen, L. Hu, J. Deng, and X. Xing, Negative thermal expansion in functional materials: Controllable thermal expansion by chemical modifications, Chem. Soc. Rev. **44**, 3522 (2015).

[50] Y. Qiao, Y. Song, A. Sanson, L. Fan, Q. Sun, S. Hu, L. He, H. Zhang, X. Xing, and J. Chen, Negative thermal expansion in $YbMn_2Ge_2$ induced by the dual effect of magnetism and valence transition, npj Quantum Mater. **6**, 1 (2021).

[51] Q. Li, K. Lin, Z. Liu, L. Hu, Y. Cao, J. Chen, and X. Xing, Chemical diversity for tailoring negative thermal expansion, Chem. Rev. **122**, 8438 (2022).